

Data Assimilation for a Kinematic Flame Model

First Year Report



Maximilian Louis Croci

Department of Engineering
University of Cambridge

Supervisor: **Prof. Matthew P. Juniper**

Adviser: **Prof. Stewart Cant**

Table of contents

1	Introduction	1
1.1	Machine Learning and Data Assimilation	1
1.2	Thermoacoustics	2
1.3	Literature Review	3
1.4	Research Objectives	4
2	The G Equation as a Kinematic Model of a Flame	5
3	Numerical Methods	11
3.1	Data Pre-processing	11
3.2	The Ensemble Kalman Filter (EnKF)	15
3.3	The LSGEN Solver	17
4	Transients in the G Equation Model	19
4.1	Linear Perturbation Analysis of the G Equation Model	19
4.2	Evidence of Transients and Implications for the EnKF Method	25
5	Proposed Alternative to EnKF using Limit Cycles and Bayesian Inference	27
5.1	The GMRES Method	27
5.2	Finding Limit Cycles with GMRES	27
5.3	Bayesian Inference for Model Selection	28
5.4	Parameter Estimation using Bayesian Inference and Limit Cycles	30
6	Conclusions and Programme of Further Research	31
7	Appendix	33
7.1	Finding $f_1(t)$, the inverse Laplace transform of $F_1(s)$	33
7.2	Finding $f_2(t)$, the inverse Laplace transform of $F_2(s)$	33
7.3	Finding $f_3(t)$, the inverse Laplace transform of $F_3(s)$	34

Table of contents

References	35
------------	----

Chapter 1

Introduction

1.1 Machine Learning and Data Assimilation

The detection and tracking of interfaces is of central importance to many computer vision techniques and applications [1]. Objects and boundaries in an image can be recognised once the image is segmented through the identification of its contours. Rapid improvements in computer processing power in the last decade and a half, combined with the notable discovery of efficient methods for training large artificial neural networks (see [2]) have allowed for a vast improvement in contour identification and image segmentation, which in turn have led to a wide variety of groundbreaking improvements in novel and existing applications, from autonomous navigation systems to facial recognition systems and image captioning software ([3], [4]).

Whereas deep artificial neural networks have demonstrated excellent object detection and recognition capabilities compared to previous methods, the process through which these go about their object detecting is often referred to as a "black box", as it is difficult to identify how the object detection predictions are being made. Moreover, these neural networks are not, in general, built with a pre-existing understanding of any physics (governing equations) behind the objects to be detected. Instead, neural networks are trained by being supplied with a set of training examples from which they learn mappings from inputs (images) to desired outputs (usually labels). In this way, neural networks can be said to provide a solely data-informed tool for object and interface detection [2].

In applications where a physics-informed tool is more desirable, alternative interface detection and tracking techniques to artificial neural networks can be used. The Kalman filter is one example of a model-based method which combines model predictions and real data in a statistically optimal way to predict the positions of objects and interfaces at any time, present or future ([5], [6]). The Kalman filter and its variants have long been implemented in

Introduction

areas where predictive models and data coexist, from trajectory estimation with the Global Positioning System (GPS) to weather forecasting and quantitative economics ([7], [6]).

Data assimilation is a mathematical discipline that seeks to statistically optimally combine theory, usually in the form of a numerical model, and observations, and the Kalman filter is one such technique. The data assimilation process usually involves taking a forecast from a current state and correcting this forecast whenever observations, however noisy, are available [8]. In this way, not only can data assimilation lead to better model forecasts but it can additionally produce estimates for model parameters which best fit the data, as well as the uncertainties in these estimates. Data assimilation techniques like the Kalman filter do not assume steady state conditions, which is especially powerful when the data is from an unsteady system, where a single estimate for the parameter values would not capture enough of the physics.

1.2 Thermoacoustics

Thermoacoustic instabilities, driven by the interaction between the heat release from the combustion process with the combustion chamber pressure waves [9], have long been a problem in jet and rocket engine design, as unacceptably large oscillations often appear during full-scale engine tests, despite being absent during part-scale tests, leading to costly re-designs. A physics-informed, data-driven model of a flame would allow for important quantities, such as the fluctuating heat release rate of the combustion process, to be estimated for a given burner geometry. This in turn would enable different geometries to be assessed for susceptibility to thermoacoustic instabilities before any physical testing, ensuring a cheaper design process.

In this report a kinematic flame model tracks the flame surface: the interface between premixed, unburnt air-fuel mixture and burnt products. A level-set based method is used to track this interface, which involves defining a level-set function over the whole flow domain and identifying the contour that corresponds to the flame surface [10]. This analytical approach to tracking the interface has advantages over other, geometric approaches where the flame surface is parametrized and discretized and its motion found by solving the laws of motion for a sufficient number of points on the surface. These advantages include better modelling of non-smooth flow features such as corners and cusps as well as topological merging and break-up [11]. This model is implemented in the Level-Set G Equation Narrow-band (LSGEN) solver, originally written by S. Hemchandra and significantly improved by I. Waugh, A. Orchini and K. Kashinath.

1.3 Literature Review

Thermoacoustic instabilities have been known and studied since as far back as the 1850s, when P. Rijke noticed sounds due to the vibration of air inside an open-ended tube [12]. Twenty years later, Lord Rayleigh published his findings on the physical mechanism behind thermoacoustic instability: velocity and pressure oscillations interact with the heat source, causing unsteady heat release. Acoustic oscillations arise when the heat release cycle and the pressure cycle are in phase [9]. The study of thermoacoustic instabilities is of particular relevance to modern day jet and rocket engines, as these are particularly vulnerable to the excitement of high-amplitude instabilities due to the high energy densities and low acoustic damping in their combustion chambers [13]. Left unaddressed, these instabilities can lead to increased heat transfer and structural vibrations, which in turn may lead to damage and ultimately failure of the engine ([14], [15]).

The G equation method of describing the surface of a flame was first introduced by F. Williams in 1985 in the study of premixed turbulent combustion [16]. This method has been used to construct an analytical model to describe the dynamic response of a laminar premixed flame with constant flame speed stabilised on the rim of a tube to velocity oscillations [17]. By considering both uniform and non-uniform velocity perturbations superimposed on a base flow velocity profile, the results show that the magnitude of heat release perturbation and its phase with respect to dynamic perturbations depend primarily on the flame Strouhal number. The model is also used to obtain a time-domain differential equation describing the relationship between the velocity perturbation and the heat release response over the entire frequency range, which is key for studying thermoacoustic oscillations. A. Dowling builds on this work to model the unsteady behaviour of a ducted flame stabilised in the wake of a bluff body [18]. Dowling shows that for linear harmonic velocity perturbations, the model allows for the time variation in the heat release rate to be calculated analytically and in excellent agreement with experimental results.

More recently, efforts have been made to combine the lightweight and easy to use analytical models previously described with real data, with very promising results. [8] introduces a data-driven, statistically rigorous framework for the assimilation of flame surface data into G Equation levels set methods, and the strengths of this framework are demonstrated. The authors use an ensemble Kalman filter (EnKF) to assimilate theoretical, laminar flame data into the G equation model in order to estimate unknown model parameters related to the prescribed velocity perturbations. With the model parameters optimally estimated from the combination of model predictions and the data, the flame surface profile can be forecasted from given starting conditions and important quantities, such as the heat release, estimated at any future time.

1.4 Research Objectives

The objectives of this work and those to follow are to **assess and demonstrate the feasibility of data assimilation techniques applied to a G equation model of a flame, using real open-source data for the Volvo burner provided by the United States Air Force** (see [19] for a description of the data). By assimilating this data, it is hoped that a physics-informed, data-driven model of the flame from a Volvo burner can be created which could be used to predict the onset of thermoacoustic instabilities in the flow. This mission is a step forward from previous data assimilation efforts on G equation-based flame models which have not yet dealt with noisy, turbulent combustion data.

Chapter 2

The G Equation as a Kinematic Model of a Flame

The equations governing the response of a flame to a time-dependent flow are derived with the following assumptions:

- The flame surface is a thin interface separating reactants (unburnt, premixed air-fuel mixture) and combustion products;
- The flame surface moves at a constant speed, the laminar flame speed, with respect to the reactants in the direction normal to the surface (the flame speed actually depends on the flame curvature);
- All effects of expansion and vorticity generation across the flame front on the flow are negligible;
- The flow field and the flame wrinkling and cusping are symmetric about the flame centre-line;
- The flame is insensitive to pressure perturbations.

The G equation is the equation that governs the behaviour of a monotonically increasing scalar field. The instantaneous flame surface position is given by a contour of this field. It is a level set method which does not rely on parametrising the flame surface. Instead, the flame surface is tracked by defining an arbitrary contour, usually $G = 0$, on which points on a grid are said to be on the surface. Defining the $G = 0$ contour to be the flame surface, regions where $G < 0$ then correspond to unburnt reactants, and regions where $G > 0$ correspond to combustion products. The actual value of the G field at a given point has no intrinsic value.

The G Equation as a Kinematic Model of a Flame

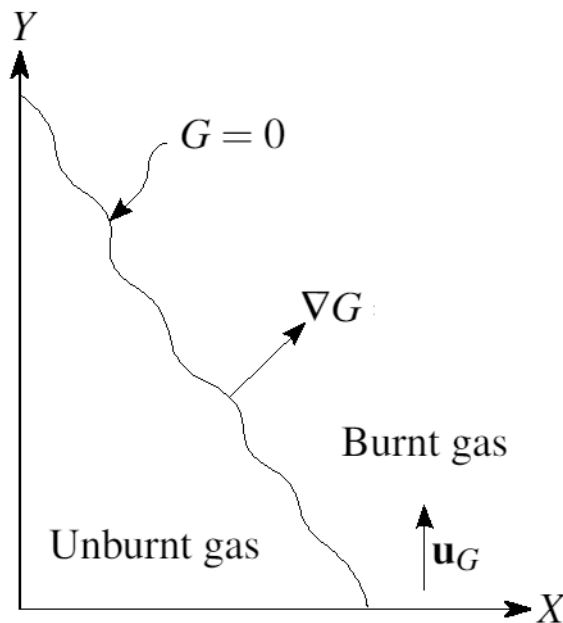


Fig. 2.1 G equation field, showing the zero contour representing the flame surface.

Instead the value is used only to distinguish between reactants, flame surface and products. Points on the zero contour satisfy:

$$G(x, y, t) = y - \psi(x, t) = 0. \quad (2.1)$$

Taking the derivative of G with respect to time leads to:

$$\dot{x} \frac{\partial G}{\partial x} + \dot{y} \frac{\partial G}{\partial y} + \frac{\partial G}{\partial t} = 0, \quad (2.2)$$

or

$$\mathbf{u} \cdot \nabla G + \frac{\partial G}{\partial t} = 0, \quad (2.3)$$

where $\mathbf{u} = [\dot{x} \ \dot{y}]^T$ is the speed of particles on the flame surface. This speed is a result of the underlying base flow \mathbf{u}_G minus a contribution from the laminar flame speed (s_L , the speed at which the flame travels against flow, burning the reactants):

$$\mathbf{u} = \mathbf{u}_G - s_L \frac{\nabla G}{|\nabla G|}. \quad (2.4)$$

Substituting this into equation 2.3 leads to:

$$\frac{\partial G}{\partial t} + \left(\mathbf{u}_G - s_L \frac{\nabla G}{|\nabla G|} \right) \cdot \nabla G = 0, \quad (2.5)$$

and so

$$\frac{\partial G}{\partial t} + \mathbf{u}_G \cdot \nabla G = s_L |\nabla G|, \quad (2.6)$$

which is known as the G equation.

By prescribing a base flow \mathbf{u}_G , the value of G at every point on a grid can be calculated, and the flame surface found (wherever $G = 0$). For example, using a steady, uniform, vertical base flow $\mathbf{u}_G = [0 \ u_G]^T$ leads to a triangular flame surface distribution, as shown by substituting (2.1) into (2.6):

$$-\cancel{\frac{\partial \psi}{\partial t}} - 0 \cdot \cancel{\frac{\partial \psi}{\partial x}} + u_G \cdot 1 = s_L \left(1^2 + \left(\frac{d\psi}{dx} \right)^2 \right)^{1/2} \quad (2.7)$$

$$u_G = s_L \left(1 + \left(\frac{d\psi}{dx} \right)^2 \right)^{1/2} \quad (2.8)$$

$$\frac{d\psi}{dx} = \pm \left(\left(\frac{u_G}{s_L} \right)^2 - 1 \right)^{1/2} = \text{const.} \quad (2.9)$$

which states that the gradient of the flame surface is a constant. Its magnitude depends on the ratio of the base flow speed to the laminar flame speed. The \pm is for each (symmetric) side of the 2-dimensional flame. Integrating this with respect to x gives:

$$\psi(x) = \pm \left(\left(\frac{u_G}{s_L} \right)^2 - 1 \right)^{1/2} x + C, \quad (2.10)$$

where C is found by using the initial condition that the flame is attached to the burner lip: $\psi(x = R) = 0$, leading to:

$$\psi(x) = \pm \left(\left(\frac{u_G}{s_L} \right)^2 - 1 \right)^{1/2} (x - R) \quad (2.11)$$

The G Equation as a Kinematic Model of a Flame

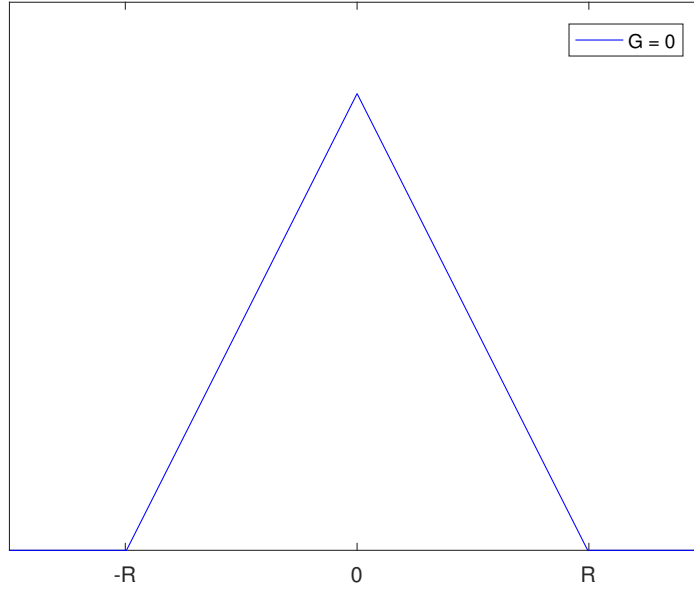


Fig. 2.2 Plot of steady flame surface.

$$\psi(x) = \begin{cases} \left(\left(\frac{u_G}{s_L} \right)^2 - 1 \right)^{1/2} (R-x) & 0 \leq x \leq R \\ \left(\left(\frac{u_G}{s_L} \right)^2 - 1 \right)^{1/2} (R+x) & -R \leq x \leq 0 . \end{cases}$$

which is plotted in figure 2.2

The base flow model used for data assimilation includes a steady, uniform vertical component and continuity-obeying perturbations in the horizontal and vertical directions:

$$\begin{aligned} \mathbf{u}_G &= u_x \mathbf{i} + u_y \mathbf{j} ; \\ u_x &= -\frac{KSt e_a}{\beta} x \cos(St(Ky - t)) ; \\ u_y &= 1 + e_a \sin(St(Ky - t)) , \end{aligned} \quad (2.12)$$

where St is the Strouhal number, e_a is the perturbation amplitude, K is the perturbation wavenumber and β is the steady state ratio of flame length to flame width, $|\partial\psi/\partial x|$. The results of a simulation of the resulting PDE are plotted figure 2.3, showing a short transient period before the oscillations become periodic and the flame system reaches a limit cycle.

The MATLAB solver requires $\psi(x)$ to be a single-valued function of x . Therefore it cannot cope with the flame looping back on itself. For the same reason, it struggles with pinch-off, at which point gradients become infinite. We therefore use this code only for

low amplitude oscillations in order to compare with the behaviour of LSGEN, our more sophisticated code.

The G Equation as a Kinematic Model of a Flame

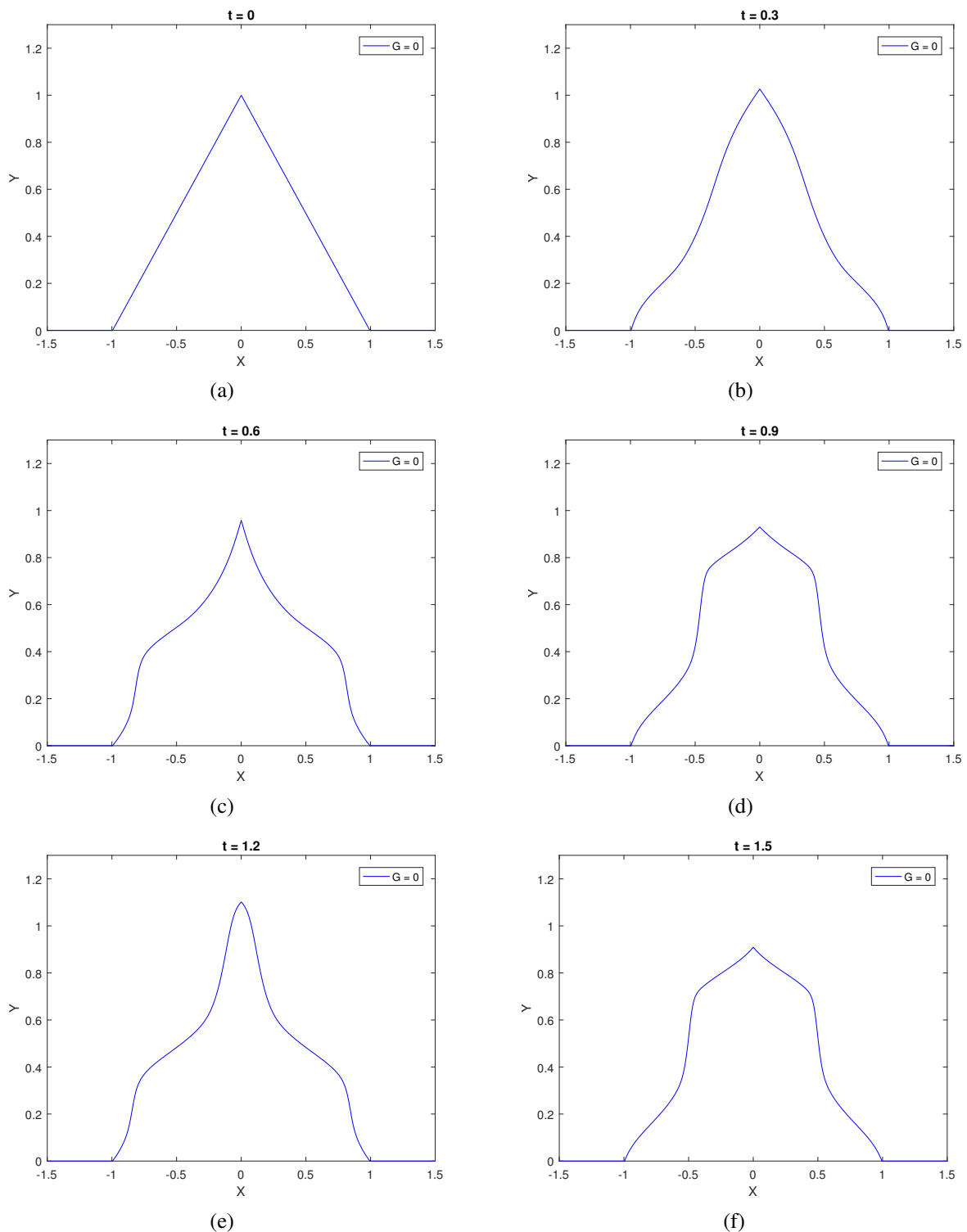


Fig. 2.3 Brute force solving of the G equation flame model in MATLAB, with parameters $R = 1.335$, $\beta = 13.2$, $St = 10$, $K = 0.5$ and $e_a = 0.1$. Note that only the $G = 0$ contour is shown, and the plots are scaled vertically by $1/\beta$.

Chapter 3

Numerical Methods

3.1 Data Pre-processing

The raw data set¹ comprises 7998 consecutive snapshots, taken at 10 kHz, of the turbulent flow downstream of a Volvo premixed gutter-stabilised flame burner. The snapshots include measurements of OH emission intensity obtained through Planar Laser Induced Fluorescence (PLIF) and measurements for axial and transverse velocity, over a 59x68 grid. Heatmaps of two OH PLIF images are shown below (the velocity components are not shown, because they are not currently used in the data assimilation process).

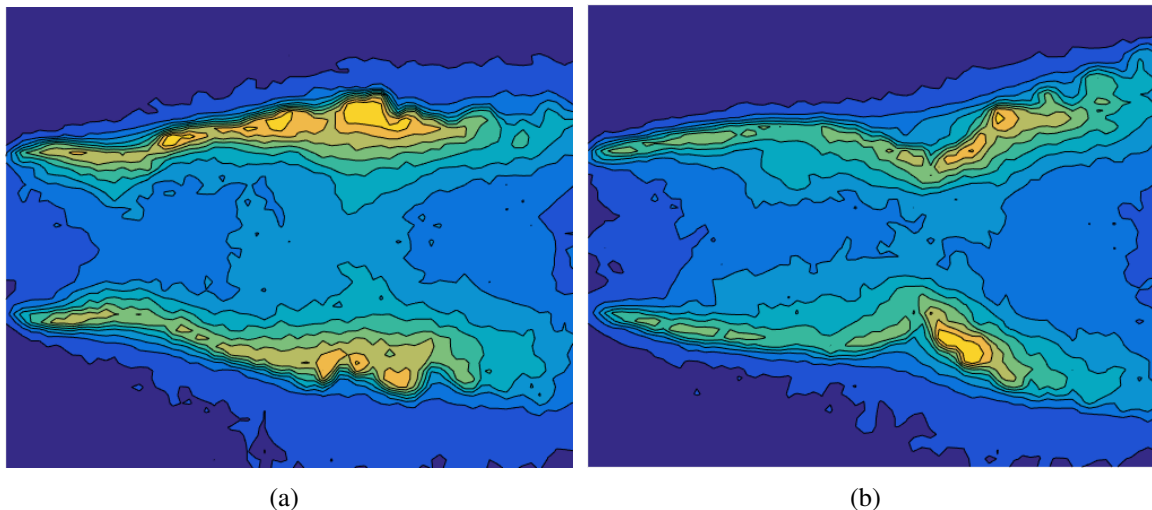


Fig. 3.1 OH PLIF images downstream of a Volvo gutter-stabilised flame.

The parameter β , the ratio of the steady state flame's length to its width can be estimated

¹This open source data set is kindly provided by B.A. Rankin, USAF.

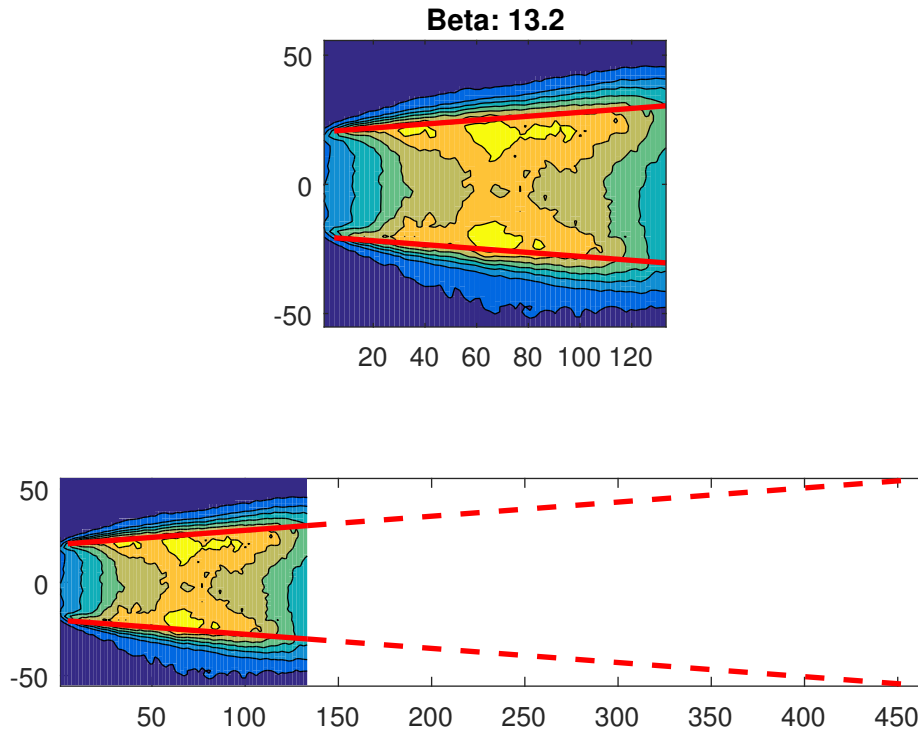


Fig. 3.2 Estimation of β , the steady state ratio of flame length to flame width.

from the data by calculating the mean OH PLIF profile and judging the flame position by eye. This process is shown in figure 2.2, giving an estimate of $\beta = 13.2$. Another important quantity is the ratio of the burner width to the duct width.

In order to assimilate this data, the positions of the flame surface must be detected from each snapshot. A number of ways to do this were tried, the most successful being a Hessian-based approach: the second derivatives of the OH signal are taken at every grid point allowing the Hessian to be constructed and its largest eigenvalue calculated, giving a measure for the maximum curvature at every point. The curvature at each point is compared to its neighbours to decide whether the point lies on the flame surface.

As can be seen from the snapshots in figure 3.1, the shape of the flame is inverted as well as horizontally aligned compared to that derived in the previous section. However, the data is transformed for use with the ensemble Kalman filter and the G equation model as follows:

1. The top half of the flame data grid is selected and flipped vertically;
2. The points on the flame surface are estimated using a Hessian based approach;
3. The coordinates of the points on the flame surface are normalised by the vertical distance between the duct wall and the burner lip;

4. The data points are reflected through $y = x$.

This process is illustrated in figures 3.3 and 3.4.

From these two figures it can be seen that the ridge detection process misses parts of the ridge. It also does not interpolate between ridge points and so these appear in bins limited by the grid size. A possible alternative to this ridge detection process would be to use computer vision algorithms such as convolutional neural networks (CNNs) to detect the ridge. When supplied with a training set of manually detected ridges, these CNNs could learn how to detect ridges in the other PLIF OH emission images with better performance than the Hessian-based approach. This will be one area of further research.

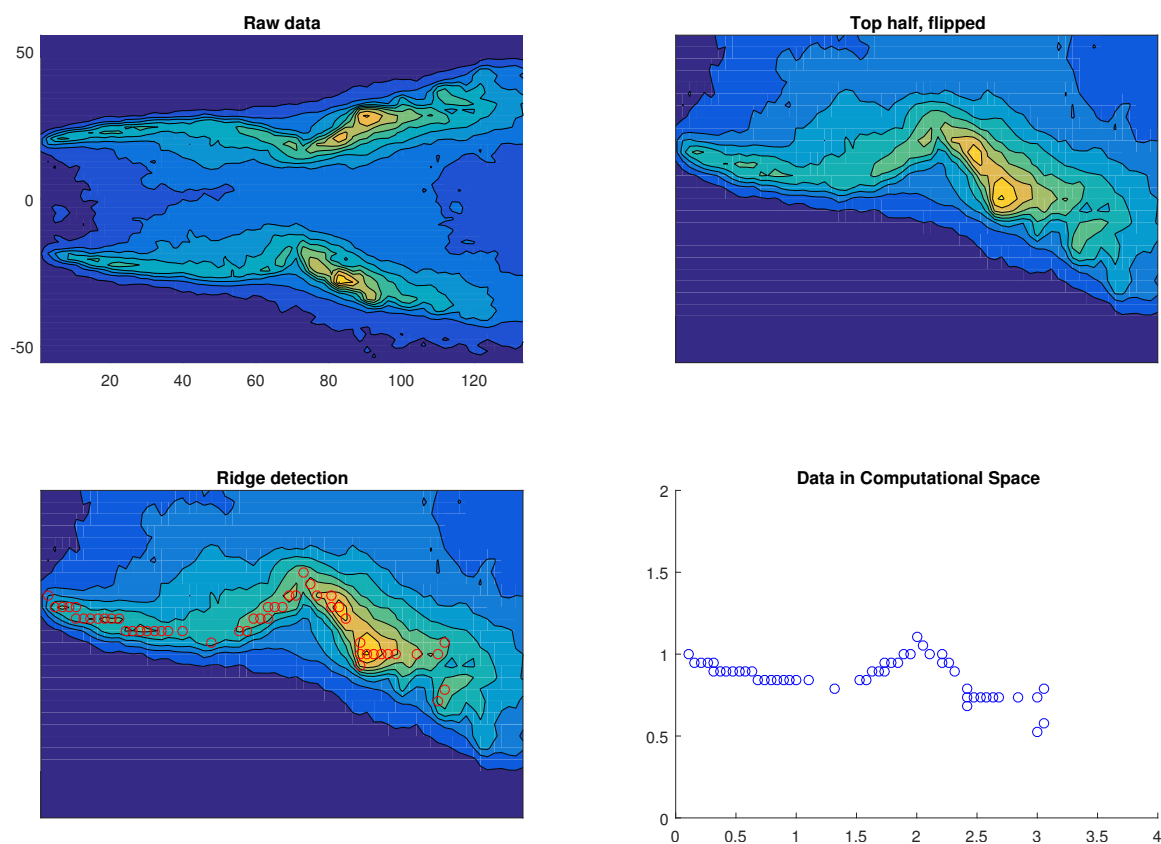


Fig. 3.3 Snapshots showing the flame surface detection and the conversion to the LSGEN computational domain (flipped and normalised by radius).

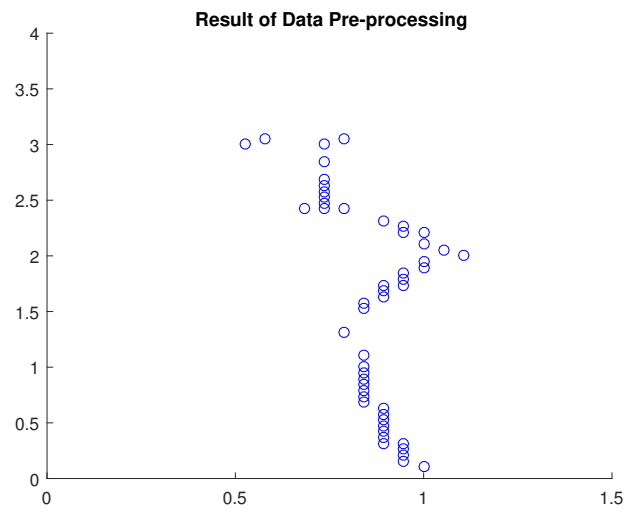


Fig. 3.4 Scatter plot of flame surface data after preprocessing. This data is used in the ensemble Kalman filter described in the next section.

3.2 The Ensemble Kalman Filter (EnKF)

The ensemble Kalman filter is an approximation of the Kalman filter, which is an algorithm that combines noisy measurements observed over time with model predictions to produce estimates of unknown variables, including the state of the system and model parameters. When using the Kalman filter, a state vector \mathbf{x} of a model is assumed to have a Gaussian probability density function (pdf) with mean vector $\boldsymbol{\mu}$ and covariance matrix $\boldsymbol{\Sigma}$:

$$p(\mathbf{x}) \propto \exp\left(-\frac{1}{2}(\mathbf{x} - \boldsymbol{\mu})^T \boldsymbol{\Sigma}^{-1}(\mathbf{x} - \boldsymbol{\mu})\right). \quad (3.1)$$

Known as the *prior*, this pdf was generated by running the model in time and must now be updated with newly available data, \mathbf{d} . These data are also assumed to have a Gaussian pdf, this time with covariance \mathbf{R} and mean $\mathbf{H}\mathbf{x}$:

$$p(\mathbf{d}|\mathbf{x}) \propto \exp\left(-\frac{1}{2}(\mathbf{d} - \mathbf{H}\mathbf{x})^T \mathbf{R}^{-1}(\mathbf{d} - \mathbf{H}\mathbf{x})\right), \quad (3.2)$$

where \mathbf{H} is known as the observation matrix (such that $\mathbf{H}\mathbf{x}$ is the value the data would be for state \mathbf{x} in the absence of data errors). For independent errors, the covariance \mathbf{R} , describing the estimate of the random errors in the data, is diagonal with the variance of the errors of the corresponding entries in the data vector as its diagonal entries:

$$[\mathbf{R}]_{j,k} \triangleq \begin{cases} \sigma_j^2 & j = k \\ 0 & j \neq k. \end{cases}$$

Bayes' theorem is used to find the *posterior* probability density of the state \mathbf{x} given the data \mathbf{d} :

$$p(\mathbf{x}|\mathbf{d}) \propto p(\mathbf{d}|\mathbf{x})p(\mathbf{x}), \quad (3.3)$$

which, given the fact that the pdf of a product of Gaussians is also Gaussian, can be written as:

$$p(\mathbf{x}|\mathbf{d}) \propto \exp\left(-\frac{1}{2}(\mathbf{x}|\mathbf{d} - \hat{\boldsymbol{\mu}})^T \hat{\mathbf{Q}}^{-1}(\mathbf{x}|\mathbf{d} - \hat{\boldsymbol{\mu}})\right), \quad (3.4)$$

and the posterior mean $\hat{\boldsymbol{\mu}}$ and covariance $\hat{\mathbf{Q}}$ are:

$$\hat{\boldsymbol{\mu}} = \boldsymbol{\mu} + \mathbf{K}(\mathbf{d} - \mathbf{H}\boldsymbol{\mu})$$

;

$$\hat{\mathbf{Q}} = (\mathbf{I} - \mathbf{K}\mathbf{H})\mathbf{Q}. \quad (3.5)$$

Numerical Methods

also known as the Kalman update formulae, and

$$\mathbf{K} = \mathbf{QH}^T (\mathbf{HQH}^T + \mathbf{R})^{-1} \quad (3.6)$$

is known as the Kalman gain. In short, the Kalman filter gives the optimal way of combining data with the current estimate of the state of a system.

The EnKF is a Monte Carlo approximation of the above filter which is more suitable to problems with a large number of variables as it avoids evolving the covariance matrix $\hat{\mathbf{Q}}$, by using a sample covariance \mathbf{C} instead. The pdf of a *prior ensemble* $\mathbf{X} = [\mathbf{x}_1, \dots, \mathbf{x}_N]$ of N members which are initially sampled from the prior distribution $p(\mathbf{x})$ is considered². The data \mathbf{d} is replicated and noise added for each ensemble to form a matrix $\mathbf{D} = [\mathbf{d}_1, \dots, \mathbf{d}_N]$ where $\mathbf{d}_i = \mathbf{d} + \boldsymbol{\varepsilon}_i$, $\boldsymbol{\varepsilon}_i \sim \mathcal{N}(\mathbf{0}, \mathbf{R})$. If the columns of \mathbf{X} form a sample from the prior probability distribution then the columns of

$$\hat{\mathbf{X}} = \mathbf{X} + \mathbf{K}(\mathbf{D} - \mathbf{HX}) \quad (3.7)$$

form a sample from the posterior. The EnKF update for the gain is then:

$$\mathbf{K} = \mathbf{CH}^T (\mathbf{HCH}^T + \mathbf{R})^{-1}, \quad (3.8)$$

which is the Kalman gain update with the state covariance \mathbf{Q} replaced by the sample covariance \mathbf{C} computed from the ensemble members:

$$\mathbf{C} = \frac{(\mathbf{X} - \mathbf{E}(\mathbf{X}))(\mathbf{X} - \mathbf{E}(\mathbf{X}))^T}{N - 1}, \quad (3.9)$$

where $\mathbf{E}(\mathbf{X}) = [E(\mathbf{X}), \dots, E(\mathbf{X})]$ is a matrix formed by repeating the ensemble mean N times.

²Although the ensemble members do not in general remain independent (as each EnKF step ties them together), they are deemed approximately so.

3.3 The LSGEN Solver

The LSGEN code solves the G equation for the flame for any given set of parameters, taking as input an initial flame surface distribution and returning as output the evolution of this flame surface through time. An example set of outputs for an initially steady flame with parameters $St = 10$, $K = 1$ and $e_a = 0.1$ is shown in figure 3.5. Note how LSGEN captures important physics such as pinch-off at the flame tip, which is crucial in the study of turbulent, large-amplitude oscillating flames.

H. Yu (CUED) augmented this code with an implementation of the EnKF so that data could be assimilated into the model and the model parameters K and e_a estimated. This was easily updated to include estimation of flame Strouhal number, St . Yu demonstrates the effectiveness of the EnKF through a "twin experiment": flame surface data is extracted from reference LSGEN outputs and fed into the EnKF, as shown in figure 3.6(c). The question is whether the EnKF works just as well with real, noisy and incomplete data..

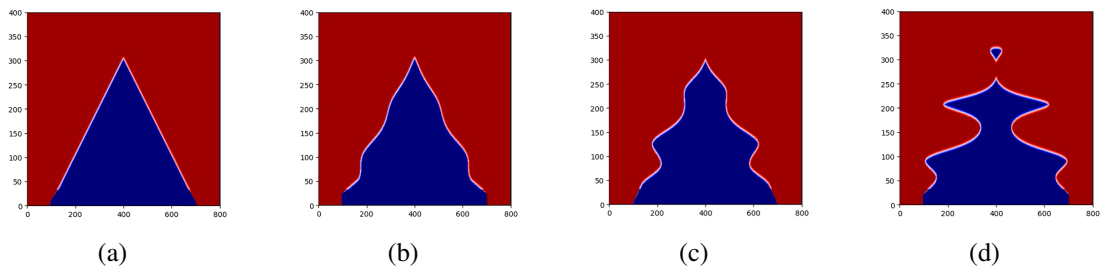


Fig. 3.5 LSGEN output flame distribution files starting from a triangular distribution.

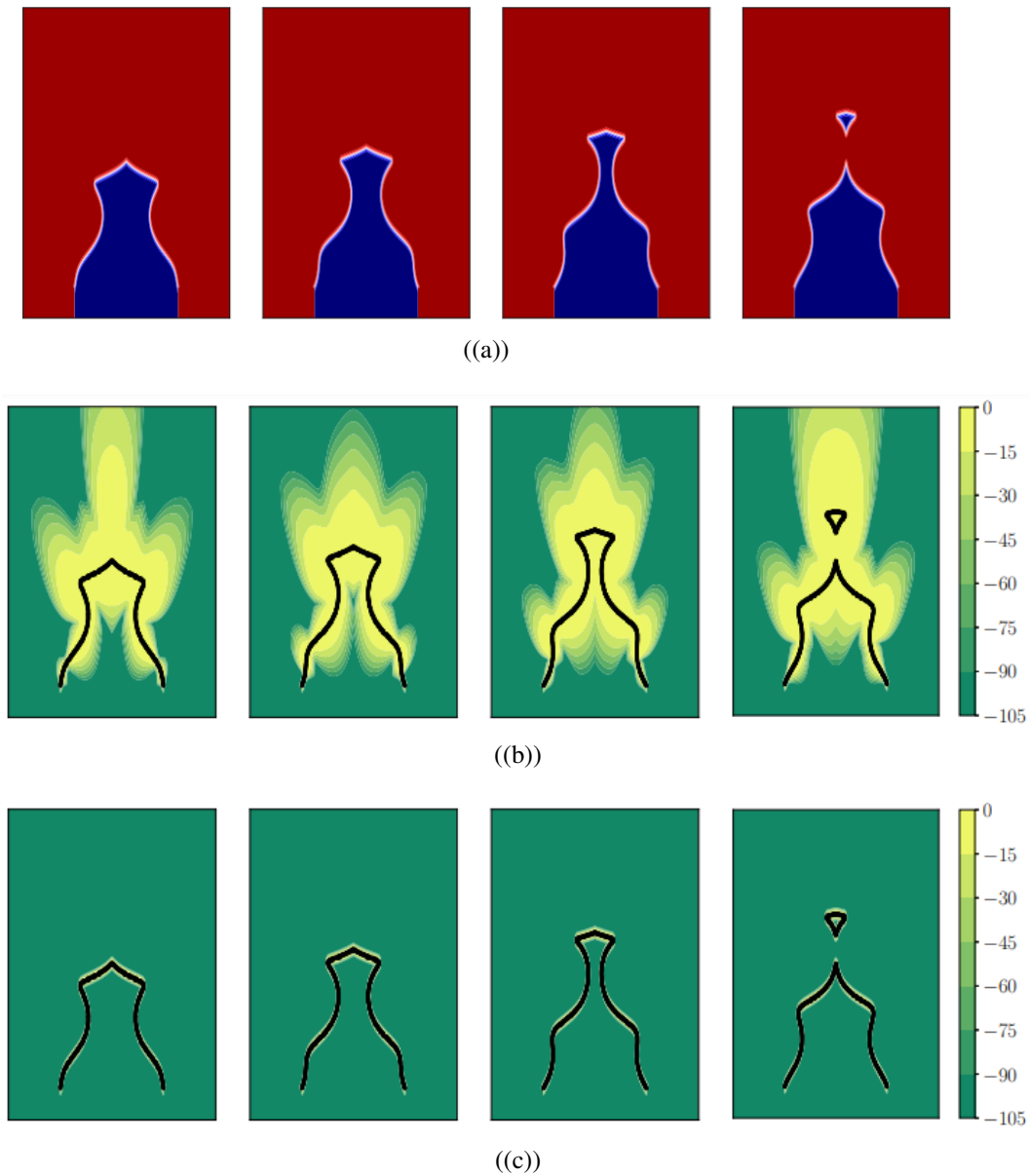


Fig. 3.6 (Top) Reference LSGEN outputs from which the surface data is extracted and fed into the EnKF. (Middle) An ensemble of independent simulations each with a unique set of parameters K and e_a are run through time, and the most likely locations (yellow regions) of the flame surface are estimated from these. No data is assimilated. (Bottom) Yu's twin experiment: data is assimilated into the ensemble of simulations and the parameters of each of these are updated accordingly, converging to the true value of K and e_a .

Chapter 4

Transients in the G Equation Model

4.1 Linear Perturbation Analysis of the G Equation Model

The following analysis is based upon work in [17], in which the results of a linear perturbation analysis of the G equation model using a purely vertical velocity perturbation are stated. This analysis considers instead a velocity perturbation with both horizontal and vertical components, and uses the same Laplace transform method suggested by [17] to solve the governing PDE.

The G equation is:

$$\frac{\partial G}{\partial t} + \mathbf{u}_G \cdot \nabla G = s_L |\nabla G| . \quad (4.1)$$

If the flame position can be represented as a single-valued function of x then $G = y - \psi(x, t) = 0$ and $\mathbf{u}_G = [u \ v]^T$. Substituting into the above gives:

$$-\frac{\partial \psi}{\partial t} + v - u \frac{\partial \psi}{\partial x} = s_L \left(1 + \left(\frac{\partial \psi}{\partial x} \right)^2 \right)^{1/2} . \quad (4.2)$$

Steady state conditions have $\psi = \bar{\psi} \neq f(t)$, $u = 0$ and $v = v_G$, which leads to:

$$v_G = s_L \left(1 + \left(\frac{\partial \bar{\psi}}{\partial x} \right)^2 \right)^{1/2} . \quad (4.3)$$

In the perturbed state $u = u'$, $v = v_G + v'$ and $\psi = \bar{\psi} + \psi'$. Substituting this into (2) gives:

$$-\frac{\partial(\bar{\psi} + \psi')}{\partial t} + v_G + v' - u' \frac{\partial(\bar{\psi} + \psi')}{\partial x} = s_L \left(1 + \left(\frac{\partial(\bar{\psi} + \psi')}{\partial x} \right)^2 \right)^{1/2} , \quad (4.4)$$

Transients in the G Equation Model

or

$$-\frac{\partial \psi'}{\partial t} + v_G + v' - u' \frac{\partial \bar{\psi}}{\partial x} = s_L \left(1 + \left(\frac{\partial(\bar{\psi} + \psi')}{\partial x} \right)^2 \right)^{1/2}. \quad (4.5)$$

To linearise the RHS requires the approximation, for small z' :

$$f(z + z') \approx f(z) + \frac{df(z)}{dz} z', \quad (4.6)$$

where

$$f(z) = (1 + z^2)^{1/2}. \quad (4.7)$$

Therefore

$$f(z + z') \approx (1 + z^2)^{1/2} + \frac{z}{(1 + z^2)^{1/2}} z'. \quad (4.8)$$

Thus

$$\left(1 + \left(\frac{\partial(\bar{\psi} + \psi')}{\partial x} \right)^2 \right)^{1/2} \approx \left(1 + \left(\frac{\partial \bar{\psi}}{\partial x} \right)^2 \right)^{1/2} + \frac{\frac{\partial \bar{\psi}}{\partial x}}{\left(1 + \left(\frac{\partial \bar{\psi}}{\partial x} \right)^2 \right)^{1/2}} \frac{\partial \psi'}{\partial x}. \quad (4.9)$$

Equation (4.5) becomes

$$-\frac{\partial \psi'}{\partial t} + v_G + v' - u' \frac{\partial \bar{\psi}}{\partial x} = s_L \left(\left(1 + \left(\frac{\partial \bar{\psi}}{\partial x} \right)^2 \right)^{1/2} + \frac{\frac{\partial \bar{\psi}}{\partial x}}{\left(1 + \left(\frac{\partial \bar{\psi}}{\partial x} \right)^2 \right)^{1/2}} \frac{\partial \psi'}{\partial x} \right), \quad (4.10)$$

or, using the steady state result:

$$-\frac{\partial \psi'}{\partial t} + v' - u' \frac{\partial \bar{\psi}}{\partial x} = \frac{s_L \frac{\partial \bar{\psi}}{\partial x}}{\left(1 + \left(\frac{\partial \bar{\psi}}{\partial x} \right)^2 \right)^{1/2}} \frac{\partial \psi'}{\partial x}, \quad (4.11)$$

and hence:

$$\boxed{\frac{\partial \psi'}{\partial t} - \bar{s}_L \frac{\partial \psi'}{\partial x} = v' + \beta u'}. \quad (4.12)$$

Where we note that $-\frac{\partial \bar{\psi}}{\partial x} \equiv \beta \geq 0$, the ratio of flame length to flame width, and define:

$$\bar{s}_L = \frac{\beta}{(1 + \beta^2)^{1/2}} s_L. \quad (4.13)$$

4.1 Linear Perturbation Analysis of the G Equation Model

We prescribe the following continuity-obeying velocity perturbations:

$$u' = -\frac{KSte_a}{\beta}x \cos(St(Ky - t)) ; \quad (4.14)$$

$$v' = e_a \sin(St(Ky - t)) . \quad (4.15)$$

Substituting these into (4.12):

$$\frac{\partial \psi'}{\partial t} - \bar{s}_L \frac{\partial \psi'}{\partial x} = e_a \sin(St(Ky - t)) - KSte_a x \cos(St(Ky - t)) . \quad (4.16)$$

This PDE is of the form:

$$\frac{\partial \psi'}{\partial t} - \bar{s}_L \frac{\partial \psi'}{\partial x} = a_1 \sin(\omega t + b) + a_2 x \cos(\omega t + b) , \quad (4.17)$$

where $a_1 = -e_a$, $a_2 = -KSte_a$, $\omega = St$ and $b = -StKy$. As this PDE is linear, we can separate the solution $\psi' = \psi'_1 + \psi'_2$:

$$\frac{\partial \psi'_1}{\partial t} - \bar{s}_L \frac{\partial \psi'_1}{\partial x} = a_1 \sin(\omega t + b) ; \quad (4.18)$$

$$\frac{\partial \psi'_2}{\partial t} - \bar{s}_L \frac{\partial \psi'_2}{\partial x} = a_2 x \cos(\omega t + b) , \quad (4.19)$$

and consider these problems individually. We now tackle PDE (4.18) by applying the Laplace transform to both sides, noting that x and y remain parameters when the Laplace transform is taken over variable t . PDE (4.18) becomes:

$$s\Psi'_1 - \psi'_1(x, t = 0) - \bar{s}_L \frac{d\Psi'_1}{dx} = a_1 \frac{s \sin b + \omega \cos b}{s^2 + \omega^2} \quad (4.20)$$

using standard results. We note that the initial condition for ψ'_1 is $\psi'_1(x, t = 0) = 0$. This leads to:

$$-\frac{s}{\bar{s}_L} \Psi'_1 + \frac{d\Psi'_1}{dx} = -\frac{a_1}{\bar{s}_L} \frac{s \sin b + \omega \cos b}{s^2 + \omega^2} . \quad (4.21)$$

This is solved using the integration factor $\exp(-sx/\bar{s}_L)$:

$$\frac{d}{dx} (e^{-sx/\bar{s}_L} \Psi'_1) = -\frac{a_1}{\bar{s}_L} \frac{s \sin b + \omega \cos b}{s^2 + \omega^2} e^{-sx/\bar{s}_L} \quad (4.22)$$

$$e^{-sx/\bar{s}_L} \Psi'_1 = -\frac{a_1}{\bar{s}_L} \frac{s \sin b + \omega \cos b}{s^2 + \omega^2} \int e^{-sx/\bar{s}_L} dx \quad (4.23)$$

Transients in the G Equation Model

$$e^{-sx/\bar{s}_L}\Psi'_1 = -\frac{a_1 s \sin b + \omega \cos b}{\bar{s}_L (s^2 + \omega^2)} \left[-\frac{\bar{s}_L}{s} e^{-sx/\bar{s}_L} + C \right] \quad (4.24)$$

or:

$$\Psi'_1 = \frac{a_1 s \sin b + \omega \cos b}{\bar{s}_L (s^2 + \omega^2)} \left[\frac{\bar{s}_L}{s} - e^{sx/\bar{s}_L} C \right]. \quad (4.25)$$

Using the initial condition $\Psi'_1(x = R, y, s) = 0$ results in:

$$\Psi'_1 = \frac{a_1 s \sin b + \omega \cos b}{\bar{s}_L (s^2 + \omega^2)} \left[\frac{\bar{s}_L}{s} - \frac{\bar{s}_L}{s} e^{-s(R-x)/\bar{s}_L} \right] \quad (4.26)$$

$$\Psi'_1 = a_1 \frac{s \sin b + \omega \cos b}{s(s^2 + \omega^2)} \left[1 - e^{-s(R-x)/\bar{s}_L} \right], \quad (4.27)$$

which is of the form:

$$\Psi'_1 = F_1(s) - e^{-cs} F_1(s). \quad (4.28)$$

This implies a solution of the form:

$$\psi'_1(x, y, t) = f_1(x, y, t) - f_1(x, y, t - c)H(t - c), \quad (4.29)$$

where $c = \frac{R-x}{\bar{s}_L}$ and $H(t - c)$ is the Heaviside step function:

$$H(t - c) = \begin{cases} 1 & t \geq c \\ 0 & t < c \end{cases}$$

and f_1 is found to be (see appendix 7.1):

$$f_1(t) = \frac{a_1}{\omega} (\cos b - \cos(\omega t + b)). \quad (4.30)$$

We next tackle PDE (4.19):

$$\frac{\partial \psi'_2}{\partial t} - \bar{s}_L \frac{\partial \psi'_2}{\partial x} = a_2 x \cos(\omega t + b).$$

Applying the Laplace transform to both sides:

$$s\Psi'_2 - \psi'_2(x, t = 0) - \bar{s}_L \frac{d\Psi'_2}{dx} = a_2 \frac{s \cos b - \omega \sin b}{s^2 + \omega^2} x. \quad (4.31)$$

This leads to:

$$-\frac{s}{\bar{s}_L} \Psi'_2 + \frac{d\Psi'_2}{dx} = -\frac{a_2 s \cos b - \omega \sin b}{\bar{s}_L (s^2 + \omega^2)} x, \quad (4.32)$$

4.1 Linear Perturbation Analysis of the G Equation Model

which is again solved using the integration factor $\exp(-sx/\bar{s}_L)$:

$$\frac{d}{dx}(e^{-sx/\bar{s}_L}\Psi'_2) = -\frac{a_2 s \cos b - \omega \sin b}{\bar{s}_L} \frac{1}{s^2 + \omega^2} x e^{-sx/\bar{s}_L} \quad (4.33)$$

$$e^{-sx/\bar{s}_L}\Psi'_2 = -\frac{a_2 s \cos b - \omega \sin b}{\bar{s}_L} \frac{1}{s^2 + \omega^2} \int x e^{-sx/\bar{s}_L} dx \quad (4.34)$$

$$e^{-sx/\bar{s}_L}\Psi'_2 = -\frac{a_2 s \cos b - \omega \sin b}{\bar{s}_L} \frac{1}{s^2 + \omega^2} \left[-\frac{\bar{s}_L}{s} x e^{-sx/\bar{s}_L} - \left(\frac{\bar{s}_L}{s}\right)^2 e^{-sx/\bar{s}_L} + C \right] \quad (4.35)$$

$$\Psi'_2 = -\frac{a_2 s \cos b - \omega \sin b}{\bar{s}_L} \frac{1}{s^2 + \omega^2} \left[-\frac{\bar{s}_L}{s} x - \left(\frac{\bar{s}_L}{s}\right)^2 + C e^{sx/\bar{s}_L} \right]. \quad (4.36)$$

The initial condition $\Psi'_2(x = R, y, s) = 0$ results in:

$$\Psi'_2 = -\frac{a_2 s \cos b - \omega \sin b}{\bar{s}_L} \frac{1}{s^2 + \omega^2} \left[-\frac{\bar{s}_L}{s} x - \left(\frac{\bar{s}_L}{s}\right)^2 + \left(\frac{\bar{s}_L}{s} R + \left(\frac{\bar{s}_L}{s}\right)^2\right) e^{-s(R-x)/\bar{s}_L} \right] \quad (4.37)$$

$$\Psi'_2 = a_2 \frac{s \cos b - \omega \sin b}{s^2 + \omega^2} \left[\frac{R}{s} \left(\frac{x}{R} - e^{-s(R-x)/\bar{s}_L} \right) + \frac{\bar{s}_L}{s^2} \left(1 - e^{-s(R-x)/\bar{s}_L} \right) \right], \quad (4.38)$$

which is of the form:

$$\Psi'_2 = F_2(s)(x/R - e^{-cs}) + F_3(s)(1 - e^{-cs}). \quad (4.39)$$

This implies a solution of the form:

$$\begin{aligned} \Psi'_2(x, y, t) = & \frac{x}{R} f_2(x, y, t) - f_2(x, y, t - c) H(t - c) \\ & + f_3(x, y, t) - f_3(x, y, t - c) H(t - c), \end{aligned} \quad (4.40)$$

and f_2 and f_3 are found to be (see appendix 7.2 and 7.3):

$$f_2(t) = \frac{a_2 R}{\omega} (\sin(\omega t + b) - \sin b); \quad (4.41)$$

$$f_3(t) = \frac{a_2 \bar{s}_L}{\omega^2} (\cos b - \omega t \sin b - \cos(\omega t + b)). \quad (4.42)$$

Transients in the G Equation Model

The overall solution is then:

$$\begin{aligned}
 \psi' = & \frac{a_1}{\omega} (\cos b - \cos(\omega t + b)) \\
 & + \frac{a_2 x}{\omega} (\sin(\omega t + b) - \sin b) \\
 & + \frac{a_2 \bar{s}_L}{\omega^2} (\cos b - \omega t \sin b - \cos(\omega t + b)) \\
 & - \frac{a_1}{\omega} (\cos b - \cos(\omega(t - c) + b)) H(t - c) \\
 & - \frac{a_2 R}{\omega} (\sin(\omega(t - c) + b) - \sin b) H(t - c) \\
 & - \frac{a_2 \bar{s}_L}{\omega^2} (\cos b - \omega(t - c) \sin b - \cos(\omega(t - c) + b)) H(t - c) .
 \end{aligned} \tag{4.43}$$

To see why this solution is transient, we note that at any point on the flame surface where $t < \frac{R-x}{\bar{s}_L}$:

$$\begin{aligned}
 \psi' = & \frac{a_1}{\omega} (\cos b - \cos(\omega t + b)) \\
 & + \frac{a_2 x}{\omega} (\sin(\omega t + b) - \sin b) \\
 & + \frac{a_2 \bar{s}_L}{\omega^2} (\cos b - \omega t \sin b - \cos(\omega t + b)) ,
 \end{aligned} \tag{4.44}$$

whereas at any point on the surface where $t > \frac{R-x}{\bar{s}_L}$, the solution is:

$$\begin{aligned}
 \psi' = & \frac{a_1}{\omega} (\cos b - \cos(\omega t + b)) \\
 & + \frac{a_2 x}{\omega} (\sin(\omega t + b) - \sin b) \\
 & + \frac{a_2 \bar{s}_L}{\omega^2} (\cos b - \omega t \sin b - \cos(\omega t + b)) \\
 & - \frac{a_1}{\omega} (\cos b - \cos(\omega(t - c) + b)) \\
 & - \frac{a_2 R}{\omega} (\sin(\omega(t - c) + b) - \sin b) \\
 & - \frac{a_2 \bar{s}_L}{\omega^2} (\cos b - \omega(t - c) \sin b - \cos(\omega(t - c) + b)) ;
 \end{aligned} \tag{4.45}$$

$$\begin{aligned}
 \psi' = & \frac{a_1}{\omega} (\cos(\omega(t - c) + b) - \cos(\omega t + b)) \\
 & + \frac{a_2}{\omega} (x \sin(\omega t + b) - R \sin(\omega(t - c) + b) + (R - x) \sin b) \\
 & + \frac{a_2 \bar{s}_L}{\omega^2} (\cos(\omega(t - c) + b) - \omega c \sin b - \cos(\omega t + b)) ,
 \end{aligned} \tag{4.46}$$

4.2 Evidence of Transients and Implications for the EnKF Method

which is different to the initial oscillation in (4.44). (4.46) applies everywhere on the flame surface after a time $t > \frac{R}{s_L}$, which is when the system has reached its limit cycle.

4.2 Evidence of Transients and Implications for the EnKF Method

As predicted by the linear perturbation analysis, for any given set of model parameters, transients are indeed found in the LSGEN solution, as shown in figure 4.1. This happens with both pinned and floating boundary conditions at the burner lip. Furthermore, if the parameters of the model are varied at any point in the simulation, transients reappear until the system reaches a new limit cycle for this new set of parameters. This same behaviour is confirmed using the MATLAB solver, as seen in figure 4.2.

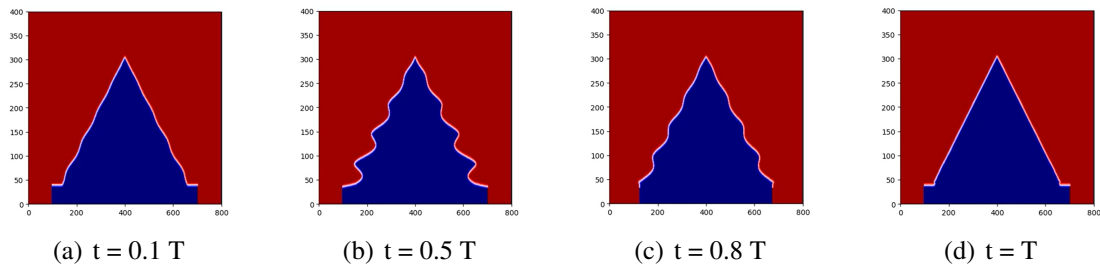


Fig. 4.1 One cycle of the transient nature in the LSGEN solution.

The implication of this fact is that when using the EnKF method, one must either study cases for which the transients are very short-lived, or the data assimilation process must be slowed down to allow for the transients to die away.

Transients in the G Equation Model

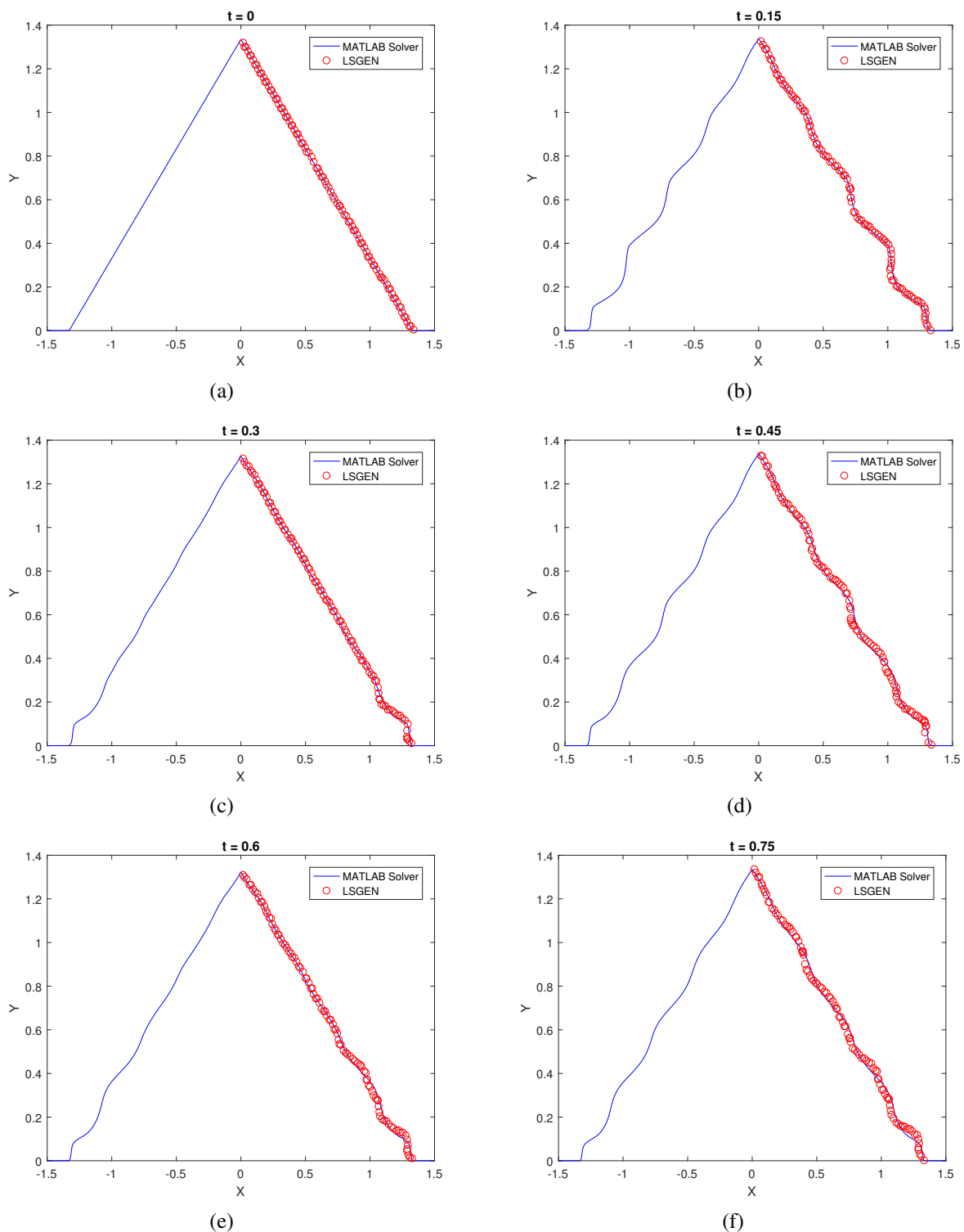


Fig. 4.2 MATLAB solution (blue solid line) to the G equation flame model with parameters $R = 1.335$, $\beta = 13.2$, $St = 40$, $K = 0.5$ and $e_a = 0.03$. The LSGEN solution (red circles) is superposed onto one half of the MATLAB solution for comparison. Note that only the $G = 0$ contour is shown, and the plots are scaled vertically by $1/\beta$. A long-lasting transient can be seen, with period of 0.3 seconds.

Chapter 5

Proposed Alternative to EnKF using Limit Cycles and Bayesian Inference

5.1 The GMRES Method

The generalised minimal residual (GMRES) method is an iterative technique used to solve for \mathbf{x} in linear algebraic problems of the form $\mathbf{Ax} = \mathbf{b}$ [20]. The method is said to be "matrix-free" because although \mathbf{A} is assumed invertible, its inverse is never calculated. Instead, GMRES uses successive matrix-vector products to define a n -dimensional Krylov subspace:

$$K_n = K_n(\mathbf{A}, \mathbf{b}) = \text{span}(\mathbf{b}, \mathbf{A}\mathbf{b}, \mathbf{A}^2\mathbf{b}, \dots, \mathbf{A}^{n-1}\mathbf{b}), \quad (5.1)$$

from which a vector $\mathbf{x}_n \in K_n$ is found which minimises the residual $\mathbf{r}_n = \mathbf{Ax}_n - \mathbf{b}$. It achieves this by first using the Arnoldi method on K_n to find a new matrix

$$\mathbf{H}_n = \mathbf{Q}_n^* \mathbf{A} \mathbf{Q}_n, \quad (5.2)$$

which is an orthogonal reduction of \mathbf{A} to Hessenberg form. \mathbf{H}_n is then used in a small least squares minimisation problem whose solution \mathbf{y}_n yields an estimate for $\mathbf{x}_n = \mathbf{Q}_n \mathbf{y}_n$.

5.2 Finding Limit Cycles with GMRES

Finding a limit cycle of the flame system described with a given set of parameter values amounts to finding a state vector \mathbf{Y} of positions on the flame surface (zero contour) to which the system returns after a known period, T . An iterative Newton method is used whereby an initial guess is made for a state $\mathbf{Y}(0)$. The resulting end state $\mathbf{Y}(T)$ after a time $t = T$ is

Proposed Alternative to EnKF using Limit Cycles and Bayesian Inference

found and the residual $\mathbf{r} = \mathbf{Y}(0) - \mathbf{Y}(T)$ is calculated. The Newton method then gives the correction $\delta\mathbf{Y}$ to be added to the initial guess in order to reduce the residual. This process is repeated until the residual reduces below a threshold. One step of this method can be expressed as

$$\mathbf{J}\delta\mathbf{Y} = -\mathbf{r} \quad (5.3)$$

where the \mathbf{J} is the Jacobian. This is of the form $\mathbf{A}\mathbf{x} = \mathbf{b}$, and can be solved with GMRES. This converges to a state \mathbf{Y} on the limit cycle as well as the period T .

5.3 Bayesian Inference for Model Selection

Our aim is to find the probability that a given model $M(\boldsymbol{\theta})$, parametrized by a vector $\boldsymbol{\theta}$ of p parameters θ_i ($i = 1$ to p), gives rise to the observed d -dimensional state (data) vector \mathbf{Y}_{obs} . To do this, we first consider the probability that a given model produced the i th observed state $\mathbf{Y}_{obs}^{(i)}$:

$$p(M(\boldsymbol{\theta})|\mathbf{Y}_{obs}^{(i)}) \quad (5.4)$$

Using Bayes' rule:

$$p(M(\boldsymbol{\theta})|\mathbf{Y}_{obs}^{(i)}) = \frac{p(\mathbf{Y}_{obs}^{(i)}|M(\boldsymbol{\theta}))p(M(\boldsymbol{\theta}))}{p(\mathbf{Y}_{obs}^{(i)})} \quad (5.5)$$

which, assuming a uniform prior $p(M(\boldsymbol{\theta})) = 1/m$ over m models leads to:

$$p(M(\boldsymbol{\theta})|Y_{obs}) = C_1 p(\mathbf{Y}_{obs}^{(i)}|M(\boldsymbol{\theta})) \quad (5.6)$$

where C_1 is a constant.

We assume the observed state undergoes a simple additive noise stochastic process:

$$\mathbf{Y}_{obs}^{(i)} = \mathbf{Y}_{M(\boldsymbol{\theta})}^{(i)} + \mathbf{WN}(\boldsymbol{\sigma}^{2(i)}) \quad (5.7)$$

5.3 Bayesian Inference for Model Selection

where $\mathbf{Y}_{M(\boldsymbol{\theta})}^{(i)}$ is the model predicted state and $\mathbf{WN}(\boldsymbol{\sigma}^{2(i)})$ is a white noise vector with variances $\boldsymbol{\sigma}^{2(i)}$. Using this equation, the probability that a state $\mathbf{Y}_{obs}^{(i)}$ arose due to model $M(\boldsymbol{\theta})$ is:

$$p(\mathbf{Y}_{obs}^{(i)} | M(\boldsymbol{\theta})) = p(\mathbf{Y}_{obs}^{(i)} | \mathbf{Y}_{M(\boldsymbol{\theta})}^{(i)}) \quad (5.8)$$

$$= \mathcal{N}(\mathbf{Y}_{M(\boldsymbol{\theta})}^{(i)}, \boldsymbol{\Lambda}^{(i)}) \quad (5.9)$$

$$= \frac{1}{\sqrt{2\pi|\boldsymbol{\Lambda}^{(i)}|}} \exp\left(-\frac{1}{2}(\mathbf{Y}_{obs}^{(i)} - \mathbf{Y}_{M(\boldsymbol{\theta})}^{(i)})^T \boldsymbol{\Lambda}^{(i)-1} (\mathbf{Y}_{obs}^{(i)} - \mathbf{Y}_{M(\boldsymbol{\theta})}^{(i)})\right) \quad (5.10)$$

$$= C_2 \exp\left(-\frac{1}{2}(\mathbf{Y}_{obs}^{(i)} - \mathbf{Y}_{M(\boldsymbol{\theta})}^{(i)})^T \boldsymbol{\Lambda}^{(i)-1} (\mathbf{Y}_{obs}^{(i)} - \mathbf{Y}_{M(\boldsymbol{\theta})}^{(i)})\right) \quad (5.11)$$

where $\boldsymbol{\Lambda}^{(i)}$ is the diagonal noise matrix:

$$[\boldsymbol{\Lambda}^{(i)}]_{j,k} = \begin{cases} \sigma_j^{2(i)} & j = k \\ 0 & j \neq k \end{cases}$$

The likelihood of all the data given the model is then:

$$p(\mathbf{Y}_{obs}^{(1:n)} | M(\boldsymbol{\theta})) = p(\mathbf{Y}_{obs}^{(1)}, \mathbf{Y}_{obs}^{(2)}, \dots, \mathbf{Y}_{obs}^{(n)} | M(\boldsymbol{\theta})) \quad (5.12)$$

$$= \prod_i p(\mathbf{Y}_{obs}^{(i)} | M(\boldsymbol{\theta})) \quad (5.13)$$

$$= C_2^n \prod_i \exp\left(-\frac{1}{2}(\mathbf{Y}_{obs}^{(i)} - \mathbf{Y}_{M(\boldsymbol{\theta})}^{(i)})^T \boldsymbol{\Lambda}^{(i)-1} (\mathbf{Y}_{obs}^{(i)} - \mathbf{Y}_{M(\boldsymbol{\theta})}^{(i)})\right) \quad (5.14)$$

$$= C_2^n \exp\left(-\frac{1}{2} \sum_i (\mathbf{Y}_{obs}^{(i)} - \mathbf{Y}_{M(\boldsymbol{\theta})}^{(i)})^T \boldsymbol{\Lambda}^{(i)-1} (\mathbf{Y}_{obs}^{(i)} - \mathbf{Y}_{M(\boldsymbol{\theta})}^{(i)})\right) \quad (5.15)$$

$$= C_2^n \exp\left(-WSSE(M(\boldsymbol{\theta}))\right) \quad (5.16)$$

where $WSSE(M(\boldsymbol{\theta}))$ is the weighted sum of squared errors under model $M(\boldsymbol{\theta})$:

$$WSSE(M(\boldsymbol{\theta})) \triangleq \frac{1}{2} \sum_i (\mathbf{Y}_{obs}^{(i)} - \mathbf{Y}_{M(\boldsymbol{\theta})}^{(i)})^T \boldsymbol{\Lambda}^{(i)-1} (\mathbf{Y}_{obs}^{(i)} - \mathbf{Y}_{M(\boldsymbol{\theta})}^{(i)}) \quad (5.17)$$

The posterior probability of the model given the data is then:

$$p(M(\boldsymbol{\theta}) | \mathbf{Y}_{obs}^{(1:n)}) = C_3 \exp\left(-WSSE(M(\boldsymbol{\theta}))\right) \quad (5.18)$$

Proposed Alternative to EnKF using Limit Cycles and Bayesian Inference

where $C_3 = C_1 C_2^n$ is a constant. C_3 can be found by the requirement that $p(M(\boldsymbol{\theta})|\mathbf{Y}_{obs}^{(1:n)})$ be a valid probability distribution i.e:

$$\sum_{M(\boldsymbol{\theta})} p(M(\boldsymbol{\theta})|\mathbf{Y}_{obs}^{(1:n)}) = 1 \quad (5.19)$$

which leads to:

$$C_3 = \frac{1}{\sum_{M(\boldsymbol{\theta})} \exp(-WSSE(M(\boldsymbol{\theta})))} \quad (5.20)$$

and finally:

$$p(M(\boldsymbol{\theta})|\mathbf{Y}_{obs}^{(1:n)}) = \frac{\exp(-WSSE(M(\boldsymbol{\theta})))}{\sum_{M(\boldsymbol{\theta})} \exp(-WSSE(M(\boldsymbol{\theta})))} \quad (5.21)$$

This states that the probability that a model $M(\boldsymbol{\theta})$ gave rise to the d observed data points in state $Y_{obs}^{(i)}$ is a weighted function of the weighted sum of squared errors, $WSSE$.

5.4 Parameter Estimation using Bayesian Inference and Limit Cycles

The observed data set $\mathbf{Y}_{obs}^{(1:n)}$ comprises n frames of one cycle of the pre-processed PLIF data. This is compared to the model prediction data set $\mathbf{Y}_{M(\boldsymbol{\theta})}^{(1:n)}$ which comprises n frames of one cycle of a limit cycle, beginning at the same phase of the cycle as the observed data and taken at identical time intervals. The WSSE is calculated by estimating the noise σ_i^2 of each observed data point in the state vector $\mathbf{Y}_{obs}^{(i)}$ and finding the distance of this point to the closest point on the 0 contour of the G field. This is done for a set of models each with different parameters, and the model with the least WSSE is selected to give the best guess of the system parameters.

Chapter 6

Conclusions and Programme of Further Research

This report has introduced the aim of creating a physics-informed, data-driven model of a flame using data assimilation. The open-source data set, provided by the United States Air Force, consists of noisy images of part of a turbulent flame downstream of a Volvo burner. Due to this turbulence, the parameters used in the G equation model of the flame vary in time. The ensemble Kalman filter (EnKF) technique to estimate these parameters was shown to require the transients in the model to dissipate, which takes time. Instead, an alternative approach to the EnKF technique is proposed which uses Bayesian inference over (transient-free) limit cycles of the system calculated by a generalised minimal residual (GMRES) method to estimate the model parameters.

The next steps will involve using the Bayesian inference and limit cycles approach for parameter estimation in three different cases:

1. estimating the parameters of a bunsen flame through the twin experiment (input data set is the output from a separate LSGEN solution with known parameters to be estimated);
2. estimating the parameters of a bunsen flame from experimental images taken at sufficiently high frequency;
3. estimating the parameters of the Volvo burner flame data set.

This will involve merging limit-cycle calculating GMRES code written by I. Waugh with the LSGEN code, followed by writing code to perform the Bayesian inference to estimate the parameters. This is expected to be completed by the end of Michaelmas 2019. Some additional data pre-processing will be necessary to extract flame surface data from the LSGEN solution and from the experimental images of a bunsen flame. The proof-of-principle

Conclusions and Programme of Further Research

exercises (1. and 2. above) are expected to be completed by Easter 2020, with exercise 3. expected to be completed by the end of the summer. Assuming satisfactory results from these, better ridge detection algorithms will be investigated, including the use of convolutional neural networks. If these out-perform the current Hessian-based approach, these will be implemented in Michaelmas 2020. At the same time, the United States Air Force will be contacted for additional data in the hope that these will validate the model predictions.

Chapter 7

Appendix

7.1 Finding $f_1(t)$, the inverse Laplace transform of $F_1(s)$

$$\begin{aligned}F_1(s) &= a_1 \frac{s \sin b + \omega \cos b}{s(s^2 + \omega^2)} \\&= a_1 \frac{\sin b}{s^2 + \omega^2} + a_1 \frac{\omega \cos b}{s(s^2 + \omega^2)} \\&= \frac{a_1 \sin b}{\omega} \frac{\omega}{s^2 + \omega^2} + \frac{a_1 \cos b}{\omega} \left(\frac{1}{s} - \frac{s}{s^2 + \omega^2} \right)\end{aligned}\tag{7.1}$$

Thus:

$$\begin{aligned}f_1(t) &= \frac{a_1 \sin b}{\omega} \sin \omega t + \frac{a_1 \cos b}{\omega} (1 - \cos \omega t) \\&= \frac{a_1}{\omega} (\cos b - \cos(\omega t + b))\end{aligned}\tag{7.2}$$

7.2 Finding $f_2(t)$, the inverse Laplace transform of $F_2(s)$

$$\begin{aligned}F_2(s) &= a_2 R \frac{s \cos b - \omega \sin b}{s(s^2 + \omega^2)} \\&= a_2 R \frac{\cos b}{s^2 + \omega^2} - a_2 R \frac{\omega \sin b}{s(s^2 + \omega^2)} \\&= \frac{a_2 R \cos b}{\omega} \frac{\omega}{s^2 + \omega^2} - \frac{a_2 R \sin b}{\omega} \left(\frac{1}{s} - \frac{s}{s^2 + \omega^2} \right)\end{aligned}\tag{7.3}$$

Thus:

$$\begin{aligned}
 f_2(t) &= \frac{a_2 R \cos b}{\omega} \sin \omega t - \frac{a_2 R \sin b}{\omega} (1 - \cos \omega t) \\
 &= \frac{a_2 R}{\omega} (\sin(\omega t + b) - \sin b)
 \end{aligned} \tag{7.4}$$

7.3 Finding $f_3(t)$, the inverse Laplace transform of $F_3(s)$

$$\begin{aligned}
 F_3(s) &= a_2 \bar{s}_L \frac{s \cos b - \omega \sin b}{s^2(s^2 + \omega^2)} \\
 &= a_2 \bar{s}_L \frac{\cos b}{s(s^2 + \omega^2)} - a_2 \bar{s}_L \frac{\omega \sin b}{s^2(s^2 + \omega^2)} \\
 &= \frac{a_2 \bar{s}_L \cos b}{\omega^2} \left(\frac{1}{s} - \frac{s}{s^2 + \omega^2} \right) - \frac{a_2 \bar{s}_L \sin b}{\omega} \left(\frac{1}{s^2} - \frac{1}{s^2 + \omega^2} \right)
 \end{aligned} \tag{7.5}$$

Thus:

$$\begin{aligned}
 f_3(t) &= \frac{a_2 \bar{s}_L \cos b}{\omega^2} (1 - \cos \omega t) - \frac{a_2 \bar{s}_L \sin b}{\omega} \left(t - \frac{1}{\omega} \sin \omega t \right) \\
 &= \frac{a_2 \bar{s}_L}{\omega^2} (\cos b - \omega t \sin b - \cos(\omega t + b))
 \end{aligned} \tag{7.6}$$

References

- [1] Yann LeCun, Y Bengio, and Geoffrey Hinton. Deep learning. *Nature*, 521:436–44, 05 2015.
- [2] David E. Rumelhart, Geoffrey E. Hinton, and Ronald J. Williams. Learning representations by back propagating errors. *Nature*, 323:533–536, 10 1986.
- [3] Christopher Bishop. Pattern recognition and machine learning. *Journal of Electronic Imaging*, 16:140–155, 01 2006.
- [4] David J. C. MacKay. *Information Theory, Inference, and Learning Algorithms*, volume 50. 01 2003.
- [5] J M. Freeman, F N. Hassan, and D Morton. Kalman filter parameter identification: a practical approach. *Transactions of The Institute of Measurement and Control*, 8:24–28, 01 1986.
- [6] P Zarchan and H Muso. Fundamentals of kalman filtering: A practical approach. 190, 01 2005.
- [7] Jean-Guy Simonato and Jin-Chuan Duan. Estimating and testing exponential-affine term structure models by kalman filter. *Review of Quantitative Finance and Accounting*, 13:111–35, 02 1999.
- [8] Juniper Matthew P. Yu, Hans and Luca Magri. Combined State and Parameter Estimation in Level-Set Methods. pages 1–51, 2019.
- [9] L Rayleigh. The explanation of certain acoustic phenomena. *Royal Institute Proceedings*, 3:536–542, 01 1878.
- [10] JA Sethian and Peter Smereka. Level set methods for fluid interfaces. *Annu. Rev. Fluid Mech*, 35:341–72, 01 2003.
- [11] Stanley Osher and Ronald P. Fedkiw. Level set methods: An overview and some recent results. *Journal of Computational Physics*, 169:463–502, 02 1970.
- [12] P. L. Rijke. Lxxi. notice of a new method of causing a vibration of the air contained in a tube open at both ends. *Philosophical Magazine Series 4*, 06 1859.
- [13] Kevin Menzies. Combustion instabilities in gas turbine engines: Operational experience, fundamental mechanisms, and modelling. *The Aeronautical Journal*, 110:394, 06 2006.

References

- [14] F Culick. Combustion instabilities in liquid-fueled propulsion systems — an overview. 01 1988.
- [15] Heinz Pitsch. Large-eddy simulation of turbulent combustion. *Annu. Rev. Fluid Mech.*, 38:453–482, 01 2006.
- [16] Alan Kerstein, William T. Ashurst, and Forman A. Williams. Field equation for interface propagation in an unsteady homogeneous flow field. *Physical review. A*, 37:2728–2731, 05 1988.
- [17] M. Fleifil, A. M. Annaswamy, Z. A. Ghoneim, and A. F. Ghoniem. Response of a laminar premixed flame to flow oscillations: A kinematic model and thermoacoustic instability results. *Combustion and Flame*, 106(4):487–510, 1996.
- [18] A P Dowling. A kinematic model of a ducted flame. *Journal of Fluid Mechanics*, 394:51–72, 1999.
- [19] Andrew W. Caswell, Brent Rankin, Bethany Huelskamp, Naibo Jiang, Amy Lynch, Vincent Belovich, and James R. Gord. Spatiotemporal characterization of flame-vortex interactions in bluff-body stabilized turbulent premixed flames using simultaneous high-repetition-rate oh-plif and piv. 01 2015.
- [20] Iain C. Waugh. PhD thesis, 2013.